Variability of fine-scale chlorophyll fronts in the Tīpaka Moana Te Moana Nui a Toi Hauraki Gulf, Aotearoa New Zealand

Alexandre Lhériau-Nice[1] and Alice Della Penna[1,2]

[1]Institute of Marine Science Te Whare Takiura Mātai Pūtaiao Moana, University of Auckland Waipapa Taumata Rau, Auckland Tāmaki Makaurau, Aotearoa New Zealand
[2]School of Biological Sciences Te Kura Mātauranga Koiora, University of Auckland Waipapa Taumata Rau, Auckland Tāmaki Makaurau, Aotearoa New Zealand

Key Points:

- Fine-scale frontal locations directly relate to wind direction and bathymetric features.
- ENSO phases contribute to fine-scale frontal dynamic, inhibiting connectivity during *El Niño* and enhancing it during *La Niña*.

Corresponding author: Alexandre Lhériau-Nice, alhe551@aucklanduni.ac.nz

Abstract

Aotearoa New Zealand's marine environment is heavily impacted by El Niño Southern Oscillation (ENSO). Little is known about the effect of ENSO on oceanographic properties in the area or their consequences on the distribution of marine organisms. Here we characterise the spatio-temporal variability of fine-scale fronts (< 10 km) in the area of Tīpaka Moana Te Moana Nui a Toi Hauraki Gulf (HG) and investigate the impact of dominant wind direction, seasonality, and ENSO phase. We processed Ocean-Land Color Instrument (OLCI) images from satellites between 2016-2022 with a fit-for-purpose version of the Belkin and O'Reilly Algorithm, specifically for frontal detection. We find coherent shifts in the position of fine-scale features, with ENSO phases alternatively separate and connect different parts of the Gulf during *El Niño* and *La Niña* respectively. Overall, fronts tend to co-locate with the 70 m and 40 m isobaths in the outer and inner HG respectively and their locations shift close or away from shore in response to changes in dominant wind direction. Furthermore, offshore fronts occurrences increase during winter and spring, and nearshore ones increase during summer and autumn. Our results sketch a first assessment of the distribution of fine-scale features that are likely to impact the distribution of important areas for pollutants dispersion and feeding areas for marine megafauna.

Plain Language Summary

Fine-scale fronts are small oceanic features less than 10 kilometres in size, that play a key role in structuring the distribution of marine organisms. Here, we investigate their impact on marine microalgae and water color in Tīpaka Moana Te Moana Nui a Toi Hauraki Gulf (HG). We use satellite images and a specialized algorithm to detect and relate the distribution of fronts with seasons, dominant wind direction, and ENSO phase (*El Niño* vs *La Niña*). ENSO phases play a role in the region, causing the fronts to alternately separate (during *El Niño*) and connect (during *La Niña*) different parts of the Gulf. This study also find there are more offshore fronts occurrences during winter and spring, and nearshore appearances during summer and autumn. The distribution of these fine-scale fronts is closely linked to wind patterns and underwater topography, particularly the 70-meter isobath outside the Gulf and the 40-meter isobath within it. Overall, this research provides insights into the spatio-temporal variability of fine-scale fronts in HG and highlights areas of potential pollutants aggregation or feeding grounds for marine megafauna.

1 Introduction

Fronts are regions where water masses having different origins and physical properties (*e.g.* temperature, salinity, nutrient concentration) meet. They are ubiquitous in open ocean and coastal regions. The properties of fronts associated with boundary currents such as the East Australian Current, Gulf Stream and Kuroshio Current have been documented for decades (Barkley, 1970; Palter, 2015; Ridgway & Hill, 2009). Recent modelling and observations suggest that fine-scaler features such as mesoscale (50 to 100 km, a week to month; McGillicuddy (2016)), submesoscale (≈ 1 km, few days; Thomas et al. (2008)), down to local sub-meter scale (> 1m , hours-day; Cowles et al. (1998)) play a key role in structuring the distribution of tracers. For example, submesoscale structures are associated with strong vertical velocities, increased phytoplankton abundance, changes in phytoplankton community composition, and estimated carbon export as documented by Mangolte et al. (2023) and in the work reviewed by Lévy et al. (2012) and Mahadevan (2016).

Home to about 1.6 million people in Auckland city alone, Tīpaka Moana Te Moana Nui a Toi Hauraki Gulf (HG) is also under the stewardship of 19 iwi (Māori tribes) authorities recognized by the Auckland Council (Council, 2021). The HG is an enclosed mass of water in the Auckland region (Aotearoa New Zealand), connected to the ocean

by 3 channels: the Jellicoe, Cradock and Colville channels, respectively between the islands of Hauturu-ō-Toi (Little Barrier), Aotea (Great Barrier) and the Coromandel Peninsula (fig.1). The dominant oceanic current in the region is the East Auckland Current (EAuC), which originates from the East Australian Current (Stevens et al., 2021), and flows north-west (NW) to south-east (SE) following the east coast of Aotearoa New Zealand. Because of the shape of the coast, winds with a component along the NW-SE axis have a strong impact on HG frontal structure (Zeldis et al., 2004). Said winds contribute to the seasonal succession of the plankton communities by switching from westerlies dominance in spring to easterlies in late summer (Zeldis et al., 2004; Zeldis & Willis, 2015). This is reflected by larger diatoms in spring replaced with dinoflagellates and nanoflagellates in late summer (Chang et al., 2003). However, while the general circulation in HG is generally understood, there is no description of the frontal patterns at the submesoscale, nor is there observation of fronts effect on biology in the Gulf.

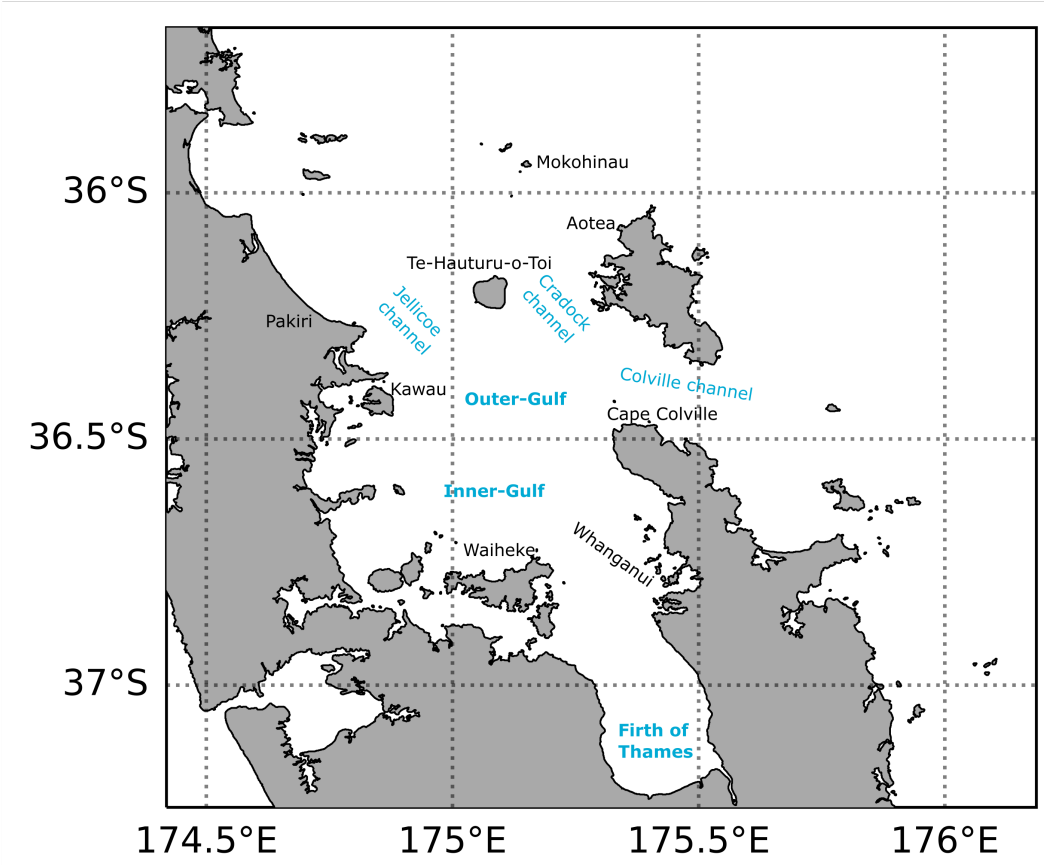

Figure 1. Map of Tīpaka Moana Te Moana Nui a Toi Hauraki Gulf.

Our aim is to identify the typical spatial patterns in frontal distribution in relations to seasons and inter-annual variability related to El Niño Southern Oscillation (ENSO), which has been suggested to be a key driver in the atmospheric and marine conditions in HG (Zeldis et al., 2004). Our main hypothesis are a significant difference in location of chlorophyll fronts between spring-summer and autumn-winter (Chang et al., 2003), as well as fronts being more intense and closer to shore during NW winds (Zeldis et al., 2004).

Fronts are most commonly studied using satellite sea surface temperature because it has been widely publicly accessible since at least the 1970's (Smith et al., 1970). Consequently, a number of front detection methods from satellite imaging rely primarily on temperature (Cayula & Cornillon, 1992; Mauzole et al., 2020), or are adapted from temperature (Liu & Levine, 2016; Miller, 2004). As we focus on the effect of fronts on the biology of the HG, like the plankton shift observed by Chang et al. (2003), we chose to use ocean color as a proxy for chlorophyll and abundance of phytoplankton in the water. Ocean colour fronts, by contrast to temperature fronts, do not only occur when two water mass of different optical properties meet, but are also generated by phytoplankton blooms on the front's edge (*active fronts*), characterised by higher chlorophyll concentration (Belkin & O'Reilly, 2009; Lévy et al., 2018).

We characterised the distribution of < 10 km fronts in HG region and investigated their temporal variability. To do so, we used Ocean and Land Colour Instrument (OLCI) at 300m spatial resolution, and optimised the Belkin and O'Reilly Algorithm (BOA, Belkin and O'Reilly (2009)) for our study area (fig.1). We then segregated data from 2016-2022 (the period for which the 300m product is available) depending on the corresponding season, dominant wind direction from a local weather station or ENSO phase. Maps were then statistically compared using the method from Levine et al. (2009). This allowed us to identify the factors that significantly contribute to HG frontal dynamic and to highlight areas where chlorophyll fronts are likely to occur.

We find that almost all selected factors (winds, season, ENSO) affect the distribution of fronts, with most of the frontal patterns being traced back to wind effect and bathymetry. The observed ocean color patterns also match know geographical segments of the Gulf, and notorious feeding grounds.

2 Methods

Overview

We compiled 6.5 years of OLCI 300m resolution maps to assess the role of wind direction, seasonality and ENSO in Tīpaka Moana Te Moana Nui a Toi Hauraki Gulf (HG, figure 1). Using an OLCI dataset at very high resolution downloaded from Copernicus Marine Services (Copernicus, 2016), we calculated maps of chlorophyll gradient in order to identify area where chlorophyll fronts are more likely. We then isolated the highest values by using a 90^{th} percentile moving window and extracted pixel lines showing the fronts positions. Afterwards, these lines where compiled over a period of 6.5 years based on winds, seasonality and ENSO to characterise the fronts patterns in HG. A panel depiction of our analysis is presented in figure 2.

We relied on the following assumptions. The first of which is that chlorophyll is a better proxy than temperature for regions of biological interest (Lévy et al., 2018). The second is that said fronts (*i.e.* chlorophyll) can be detected using the Belkin and O'Reilly Algorithm (BOA), showing potential relation with the seafloor topography (Belkin & O'Reilly, 2009). Third, the variability of submesoscale structure allow for extra productivity (Lévy et al., 2012) which will change the position and/or type of plankton on an temporal basis (Chang et al., 2003). Fourth, said variability contribution to front patterns can be analysed based on a single season/wind/ENSO phase.

2.1 High resolution ocean colour data from OLCI

The data used in this study are Ocean and Land Colour Instrument (OLCI) images taken from the mission Sentinel 3-A and B, and provided by Copernicus under product ID *009_103* (Copernicus, 2016). This data product combines ocean color, chlorophyll concentration and turbidity measured by sensors on satellites Sentinel-3A and 3B (Colella

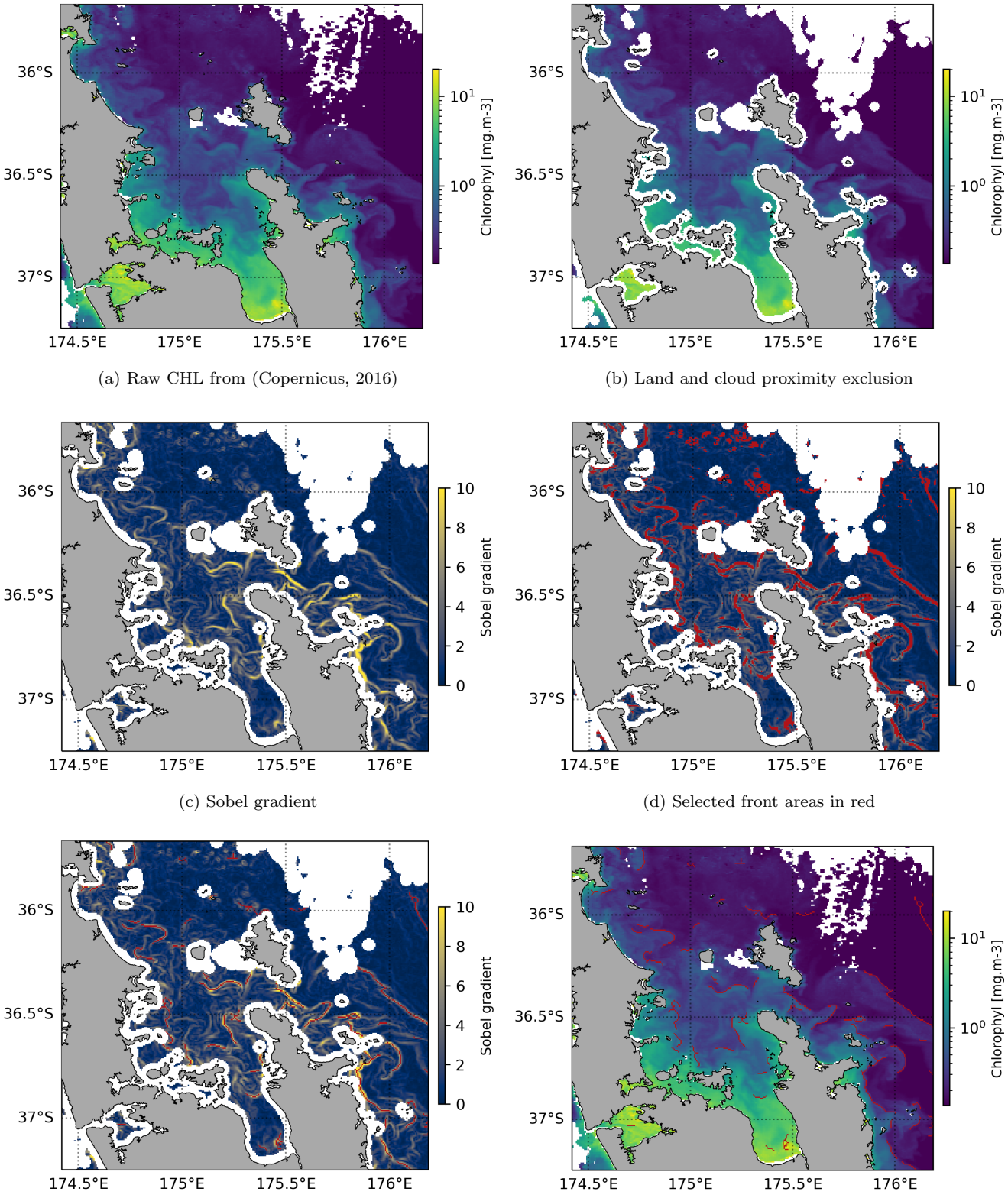

(a) Raw CHL from (Copernicus, 2016)

(b) Land and cloud proximity exclusion

(c) Sobel gradient

(d) Selected front areas in red

(e) Morphological thining to lines

(f) Overlap of the front lines with the CHL

Figure 2. Panel showing the process followed by the pyBOA.

et al., 2022; Copernicus, 2016) and is available at 300 m spatial resolution starting from May 25^{th} 2016.

2.2 Front detection

Before using the pyBOA, we applied a log function of the chlorophyll (CHL) values and removed all values superior to 30mg.m^{-3} as per Copernicus recommendation (EUMETSAT, 2021).

Chlorophyll fronts do not only occur when water masses of different optical properties meet, but are also the result of phytoplankton blooms on the front's edge. Both results in high chlorophyll zone although the second occurrence appears as like a localised chlorophyll maximum (see fig.4 in Belkin and O'Reilly (2009)) rather than gradient like as describe for temperature fronts (Cayula & Cornillon, 1992). These important blooms are likely triggered by the above mentioned vertical mixing (Lévy et al., 2012; Mahadevan, 2016), and contribute to the creation of three water-masses of different chlorophyll concentration at fronts, one on each side and one at the front itself (see fig.4 in Belkin and O'Reilly (2009)). This structure, different from the one expected for temperature fronts (two population, one on each side), make the usual edge detection like Cayula and Cornillon (1992) less effective. For that reason, we adapted the algorithm from Belkin and O'Reilly (2009), which is designed to detect these 3-population structures, to our study site.

This fit-for-purpose version of the BOA algorithm (*i.e.* pyBOA as it was built in python 3.9) (Belkin & O'Reilly, 2009; Galuardi, 2012; Lin et al., 2019) has a number of modifications and additions. The first modification from the original BOA algorithm is the identification of local extrema. While the original algorithm (Belkin & O'Reilly, 2009; Lin et al., 2019) uses a slicing method on the 5∗5 window, effectively masking 8 out of the 25 values, in this study we use an approach similar to Galuardi (2012) by assessing whether the center of each window is equal to the max/min of the window itself. In addition, we included a cloud and land proximity filter to avoid artefacts created by empty cell vicinity, and we defined a rolling window front threshold allowing to detect nearshore as well as offshore. This means that the pixels near land are removed and the threshold is similar (here 90^{th} percentile) but not equal (near shore vs far from shore). Finally, we included a delineation process to go from identified pixels groups to lines following the gradient.

In practice, we extracted the local CHL extrema in each 5∗5 pixels window before applying a median filter on a 3∗3 pixels window. Following the median filter, a Sobel edge detection method is used, corrected to take into account the distance distortion using the Haversine formula. Clouds and land vicinity are masked by marking as NaN all values that are 4 pixels ($\approx$ 1.2 km) within land or cloud vicinity. The front categorisation thresholds are then defined on the result of the Sobel gradient using a 64∗64 pixels rolling window, in which the values above the 90^{th} percentile are flagged as on a *front* (similar to Lehahn et al. (2007)). Experimenting with other window sizes (*e.g.* 16∗16 and 32∗32) suggested that this the optimal size window for our study region as it maximize delineation and minimize artefacts. The flags are then cleaned using two iteration of morphological thinning (from group to line keeping the central shape), spur removal (get rid of terminal pixels) and artefact removal with features less than 7 pixels long considered artefacts, with a cross-shaped dilation and holes removal in-between both iteration. The removal of features smaller than 7 pixels mitigates the impact of artefacts from the smaller kernel of the pyBOA (3∗3).

2.3 Group segregation by wind direction, season, and ENSO phase

Upon detection, the fronts are saved in binary form with 1 being the *front* category and 0 the *non-front*. Different groups are then formed based on one of the subsequent criteria: dominant wind direction (8 groups), season (four groups), ENSO oscillation phase (three groups). The dominant wind direction was calculated on a daily basis using the hourly data of the Mokohinau islands station (fig.1) from Meteorological Service of New Zealand Ltd and separated between the four cardinals (North, South, East, West) and four sub-components (North-West, NW; South-West, SW; South-East, SE; North-East, NE). September-November were classified as Spring; December-February as Summer; March-May as Autumn; June-August as Winter. The Southern Oscillation Index (SOI) provided by NOAA (2022) was used to determine the state of the ENSO oscillation like so: $SOI < -0.5$, *El Niño*; $-0.5 \leq SOI \leq 0.5$, Neutral; $0.5 < SOI$, *La Niña*. Upon segregation, each binary file is passed through a 5∗5 Gaussian kernel accounting for finer-scale variability (e.g. tides; Hu et al. (2016)) and detection errors, and the resulting map is normalized in order to keep the *front* category value equal to 1. The results are aggregated using the P_{fronts} from equation 1 to produce single factor frontal probability maps (see figure 3).

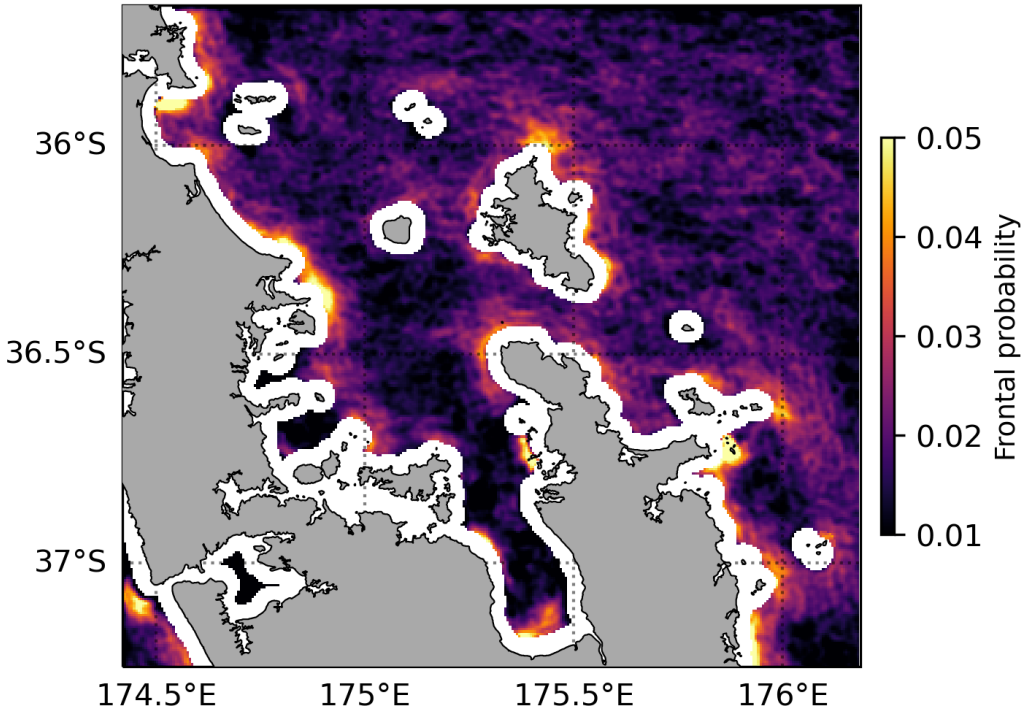

Figure 3. Probability map in Tīpaka Moana Te Moana Nui a Toi Hauraki Gulf.

2.4 Compilation of probability maps

We pooled data from 2442 days following P_{front} from equation 1:

$$P_{front_i} = \frac{\sum_1^n front\ category_i}{\sum_1^n non-empty\ values_i} \tag{1}$$

Where i a given pixel and n the number of days considered.

2.5 Statistical analysis

The analyses mentioned in section 2.4 result in one probability map showing the probability of detecting fronts over 2442 days (fig.3), as well as probability maps based on individual environmental variables (fig.4, 5, 6), with each corresponding group (wind, season, ENSO). See subdivisions details in table 1.

Table 1. Number of fronts pixels, valid pixels, and front to valid ration for each factor. The grey lines correspond to the lines with non-significant p-values on the t-test.

Group	Factor	n days	Fronts	Valid	Ratio (F/V)
Wind	North	7	268	$1.51{\cdot}10^{5}$	$1.78\ 10^{-3}$
Wind	North-East	97	9975	$2.84{\cdot}10^{6}$	$3.51{\cdot}10^{-3}$
Wind	East	312	$3.65{\cdot}10^{4}$	$1.12{\cdot}10^{7}$	$3.25{\cdot}10^{-3}$
Wind	South-East	305	$6.83{\cdot}10^{4}$	$1.45{\cdot}10^{7}$	$4.70{\cdot}10^{-3}$
Wind	South	271	$9.48{\cdot}10^{4}$	$1.81{\cdot}10^{7}$	$5.24{\cdot}10^{-3}$
Wind	South-West	536	$1.40{\cdot}10^{5}$	$3.31{\cdot}10^{7}$	$4.21{\cdot}10^{-3}$
Wind	West	558	$1.02{\cdot}10^{5}$	$2.29{\cdot}10^{7}$	$4.48{\cdot}10^{-3}$
Wind	North-West	154	$2.76{\cdot}10^{4}$	$6.19{\cdot}10^{6}$	$4.46{\cdot}10^{-3}$
Season	Spring	637	$1.41{\cdot}10^{5}$	$3.14{\cdot}10^{7}$	$4.50{\cdot}10^{-3}$
Season	Summer	572	$1.56{\cdot}10^{5}$	$3.36{\cdot}10^{7}$	$4.65{\cdot}10^{-3}$
Season	Autumn	589	$1.25{\cdot}10^{5}$	$2.89{\cdot}10^{7}$	$4.34{\cdot}10^{-3}$
Season	Winter	644	$9.93{\cdot}10^{4}$	$2.50{\cdot}10^{7}$	$3.97{\cdot}10^{-3}$
SOI	*El Niño*	581	$1.24{\cdot}10^{5}$	$2.87{\cdot}10^{7}$	$4.32{\cdot}10^{-3}$
SOI	*La Niña*	883	$1.80{\cdot}10^{5}$	$4.16{\cdot}10^{7}$	$4.32{\cdot}10^{-3}$

To compare maps, we used the statistical approach described by Levine et al. (2009). The idea behind this approach (*jackknife*) is that by removing one factor (*e.g.* winter if we are considering a seasonal study), it is possible to evaluate the impact of said factor on the overall map. For each factor, we created a jackknife map by removing the days associated with that factor from the full dataset (front and valid pixels alike) as seen in Eq.2:

$$Jackknife_{factor} = \frac{Front_{data} - Front_{factor}}{Valid_{data} - Valid_{factor}} \tag{2}$$

Where $Front_{data}$ is the probability of observing a front for a pixel in the full dataset, $Front_{factor}$ the probability of observing a front for a pixel in the $factor$ group, $Valid_{data}$ the number of non-empty observation for one pixel in the full dataset, $Valid_{factor}$ the number of non-empty observation for one pixel in the $factor$ group. Each $Jackknife_{factor}$ is then transformed into a $\delta_{factor} = Jackknife_{factor} - P_{front_{data}}$ map (where $P_{front_{data}}$ is P_{front} for the full dataset). The ENSO calculation was done differently as the SOI includes a *Neutral* factor that in this analysis we consider as the norm. Hence, the $Jackknife_{factor}$ step was passed and all ENSO factors where treated using a simple delta of probability like so: $\delta_{factor} = P_{front_{factor}} - P_{front_{Neutral}}$.

This process created $n = 12$ jackknife maps (four seasons, 8 wind orientations) and $n = 14$ δ_{factor} maps (adding two SOI) of identical dimensions (285∗318 pixels), transformed into single column table of 90'630 lines for statistical analysis.

The resulting maps are paired with the complete dataset then compared using a Student t-test with the null hypothesis being the absence of difference between the full dataset and one jackknife map. As the maps of HG contain a large number of pixels (90'630

pixels), the δ_{factor} maps were assumed to follow a normal distribution. The results from each t-test (Student t, degree of freedom and p-value) are summarized in table 2. General statistics where also generated including the mean, standard error and 75% confidence interval limits (table 2).

This approach is based on a pixel-by-pixel analysis and only give information on the general contribution of a variable (Levine et al., 2009). To visualise how each factor impacted the spatial distribution of fronts, we showed spatial changes by selectively isolating the values of every δ_{factor} outside of the 75% confidence interval. Because of how these δ variables are constructed, the minimum δ values correspond to the areas where the $Jackknife_{factor}$ values are the highest (i.e., where each factor has maximum impact), and vice versa. Hence, the value of δ are multiplied by -1 to facilitate interpretation. For example in figure 5d, a high value of $-\delta$ in the area of Kawau means there is a higher frontal presence there in Summer.

3 Results

3.1 General frontal probability

Tīpaka Moana Te Moana Nui a Toi Hauraki Gulf (HG) channels and near-shore regions (fig.3) are characterised by higher frontal probabilities with hotspots north of Aotea (36° South, 175.45° East; average value ≈ 0.05), around Cape Colville (36.5°S-175.25°E; average value ≈ 0.035), North of Kawau (36.4°S-174.7°E; average value ≈ 0.05), West of Whanganui (36.75°S-175.45°E; average value ≈ 0.035), north of Waiheke, and in the Firth of Tames (37.2°S-175.4°E; average value ≈ 0.045). Three lines of high probabilities stand out, one between Kawau and Waiheke (average value ≈ 0.035), the second originating from Cape Colville to Kawau (average value ≈ 0.03), and lastly a more faint one between Cape Colville and Waiheke (average value ≈ 0.025). These sets of fronts effectively structure the gulf in 3 sections, one being the Firth of Thames, another in the triangle Waiheke-Kawau-Cape Colville usually referred to as the inner gulf (Gaskin, 2021) and the last one North of the line Kawau-Cape Colville usually identified as outer gulf (Gaskin, 2021).

3.2 Factor differences

3.3 Spatio-temporal variability

All results presented in figures 4, 5 and 6 are paired showing the probability of a factor (*e.g.* spring, fig.5a) and the associated $-\delta$ (*e.g.* spring, fig.5b).

3.3.1 Wind direction

Out of the 8 wind directions considered for the analysis, only 4 are detailed here. The first two are North-West (NW, fig.4a-4b) and South-East (SE, fig.4c-4d) as these are expected to promote upwelling (NW) and downwelling (SE) (Zeldis et al., 2004). The other wind origins we considered are West (fig.4e-4f) and East (fig.4g-4h) as they both have components close to the NW-SE axis, and are more frequent than meridional winds (tab.1). Among the winds considered, the maxima in frontal probability are: 0.1511 for NW; 0.1850 for SE; 0.1127 for westerlies; and 0.1261 for easterlies.

Dominant NW winds (fig.4a-4b) correspond to increases in frontal probability in the center of the inner and outer Gulf, as well as across the Jellicoe and Cradock channels. North of Aotea and north of Kawau are two areas that shows important patches of decreased probability. This wind origin is evaluated non-significant by the Student t-test result (tab.2) and the values of the jackknife are of smaller magnitude compared to other wind origins with higher occurrences. For example, NW winds $-\delta$ range from -0.0045

Table 2. Summary of t-test analysis of jackknifes maps highlighting major contribution of wind orientation, season, and ENSO phase in Tīpaka Moana Te Moana Nui a Toi Hauraki Gulf. Factors resulting in non-significant p-values are grey colored.

Factor	Mean	σ	Student t	DF	p-value	CI inf	CI sup	SE
North	0.0180	0.0071	-0.34	50170	0.734	$-6.90{\cdot}10^{-7}$	$4.86{\cdot}10^{-7}$	$3.00{\cdot}10^{-7}$
North.East	0.0180	0.0071	-4.39	50170	< 0.01	$-1.14{\cdot}10^{-5}$	$-4.35{\cdot}10^{-6}$	$1.79{\cdot}10^{-6}$
East	0.0181	0.0070	-15.93	50170	< 0.01	$-6.49{\cdot}10^{-5}$	$-5.07{\cdot}10^{-5}$	$3.63{\cdot}10^{-6}$
South.East	0.0179	0.0070	19.52	50170	< 0.01	$9.31{\cdot}10^{-5}$	$1.14{\cdot}10^{-4}$	$5.30{\cdot}10^{-6}$
South	0.0179	0.0070	15.95	50170	< 0.01	$8.31{\cdot}10^{-5}$	$1.06{\cdot}10^{-4}$	$5.94{\cdot}10^{-6}$
South.West	0.0181	0.0074	-14.04	50170	< 0.01	$-1.22{\cdot}10^{-4}$	$-9.18{\cdot}10^{-5}$	$7.60{\cdot}10^{-6}$
West	0.0181	0.0074	-7.06	50170	< 0.01	$-5.91{\cdot}10^{-5}$	$-3.34{\cdot}10^{-5}$	$6.55{\cdot}10^{-6}$
North.West	0.0180	0.0071	-1.07	50170	0.285	$-9.02{\cdot}10^{-6}$	$2.65{\cdot}10^{-6}$	$2.98{\cdot}10^{-6}$
Spring	0.0174	0.0075	72.69	50170	< 0.01	$6.15{\cdot}10^{-4}$	$6.49{\cdot}10^{-4}$	$8.69{\cdot}10^{-6}$
Summer	0.0175	0.0070	49.82	50170	< 0.01	$4.90{\cdot}10^{-4}$	$5.31{\cdot}10^{-4}$	$1.02{\cdot}10^{-5}$
Autumn	0.0180	0.0072	-1.29	50170	0.198	$-2.90{\cdot}10^{-5}$	$6.00{\cdot}10^{-6}$	$8.92{\cdot}10^{-6}$
Winter	0.0191	0.0077	-120.88	50170	< 0.01	$-1.07{\cdot}10^{-3}$	$-1.04{\cdot}10^{-3}$	$8.75{\cdot}10^{-6}$
El Niño	0.0176	0.0085	18.30	50170	< 0.01	$3.79{\cdot}10^{-4}$	$4.69{\cdot}10^{-4}$	$2.32{\cdot}10^{-5}$
La Niña	0.0179	0.0082	6.52	50170	< 0.01	$7.81{\cdot}10^{-5}$	$1.45{\cdot}10^{-4}$	$1.71{\cdot}10^{-5}$

to 0.0029 while westerlies $-\delta$ range from -0.0069 to 0.015. When SE winds dominate (fig.4c-4d), frontal probability increases along the 40m isobath, off of Colville Cape toward Kawau, across the Cradock channel and north of Te-Hauturu. Small patches of decreased probability are present off the coast of Pakiri and in the center of the inner-Gulf. The impact of SE winds is identified as significant, with a mean of 0.0179 and a σ of 0.007. Westerlies (fig.4e-4f) create important decreases along the 40m and 70m isobath and a strong increase from Pakiri into the inner Gulf by the Jellicoe channel. Westerlies are significant as well in the t-test with a mean of 0.0181 and a σ of 0.0074. Easterlies winds (fig.4g-4h) show increased probability on a line between Kawau and Cape Colville, and between the 70m and 100m isobath north of Te-Hauturu-o-toi. Areas of decreased probability are noticeable by Pakiri, in the Cradock channel and north of the Mokohinau islands. Easterlies are significant on the t-test, with a mean of 0.0181 and a σ of 0.007.

3.3.2 Seasons

Maxima in frontal probability are: 0.1069 in spring; 0.2112 for summer; 0.1282 during autumn; and 0.1317 in winter. In spring frontal probability decreases inside the inner Gulf as well as along the 100m isobath compared to other seasons (fig 5a-5b). Local increases are observed in four areas of the outer Gulf: Jellicoe and Cradock channels, north of Waiheke and Cape Colville. General increase is visible offshore past the 100m isobath. This season is significant in the t-test with a mean of 0.0174 and a σ of 0.0075. In summer (fig 5c-5d) frontal probability is patchy on the 70m isobath and beyond, with numerous patches of increases and decreases probability. Probability increases around Kawau, north Waiheke and Cape Colville show greater intensity than in spring. Summer is also significant in the t-test with a mean of 0.0175 and a σ of 0.007. In Autumn (fig 5e-5f) high front probability areas shift to follow the 40m isobath and flow from Kawau out to the Colville channel. Out of the Gulf, high probabilities are mostly present between the 70 and 100m isobath. Past the 100m isobath, important decrease start to show-up, as well as in the Cradock channel and near Pakiri. This season is however non-significant in the Student t-test result (tab.2). Winter (fig 5g-5h) is characterised by massive decrease in frontal probability all over the study area, and it is especially noticeable around Kawau, north of Waiheke, Whanganui and Cape Colville. We also observe a more subtle general decrease past the 100m isobath. Two increases strands can be seen in the inner Gulf and between the 70 and 100m isobath (like in autumn). Winter turns out significant in the t-test with a mean of 0.0191 and a σ of 0.0077.

3.3.3 ENSO

Maxima in frontal probability are: 0.1187 for *El Niño* periods, and 0.1271 during *La Niña* events.

During *El Niño* periods (figures 6a-6b), lines of increased probability can be seen at the 40m isobath separating the Firth of Thames and the inner Gulf, and east of Kawau separating the inner Gulf and outer Gulf. Additionally, increases are visible between the north of Pakiri's coast and the Mokohinau islands, and north-west of Aotea. There are noticeable decreases in the center of the inner Gulf and on Pakiri's coastline.

During *La Niña* events (figures 6c-6d), higher values of frontal probabilities along the 40m isobath remained, clearly separating the Firth of Thames and the inner Gulf. However, the eastern line from Kawau disapear, promoting mixing between the inner and outer Gulf. The line of fronts previously observed between the north of Pakiri's coast and the Mokohinau islands moved towards 70m isobath, and a second increase probability line appear parallel to the first, north of the Mokohinau islands.

Both *El Niño* and *La Niña* events are significant under the t-test, with a respective mean of 0.0176 and 0.0179, with associated σ equal to 0.0085 and 0.0082 respectively.

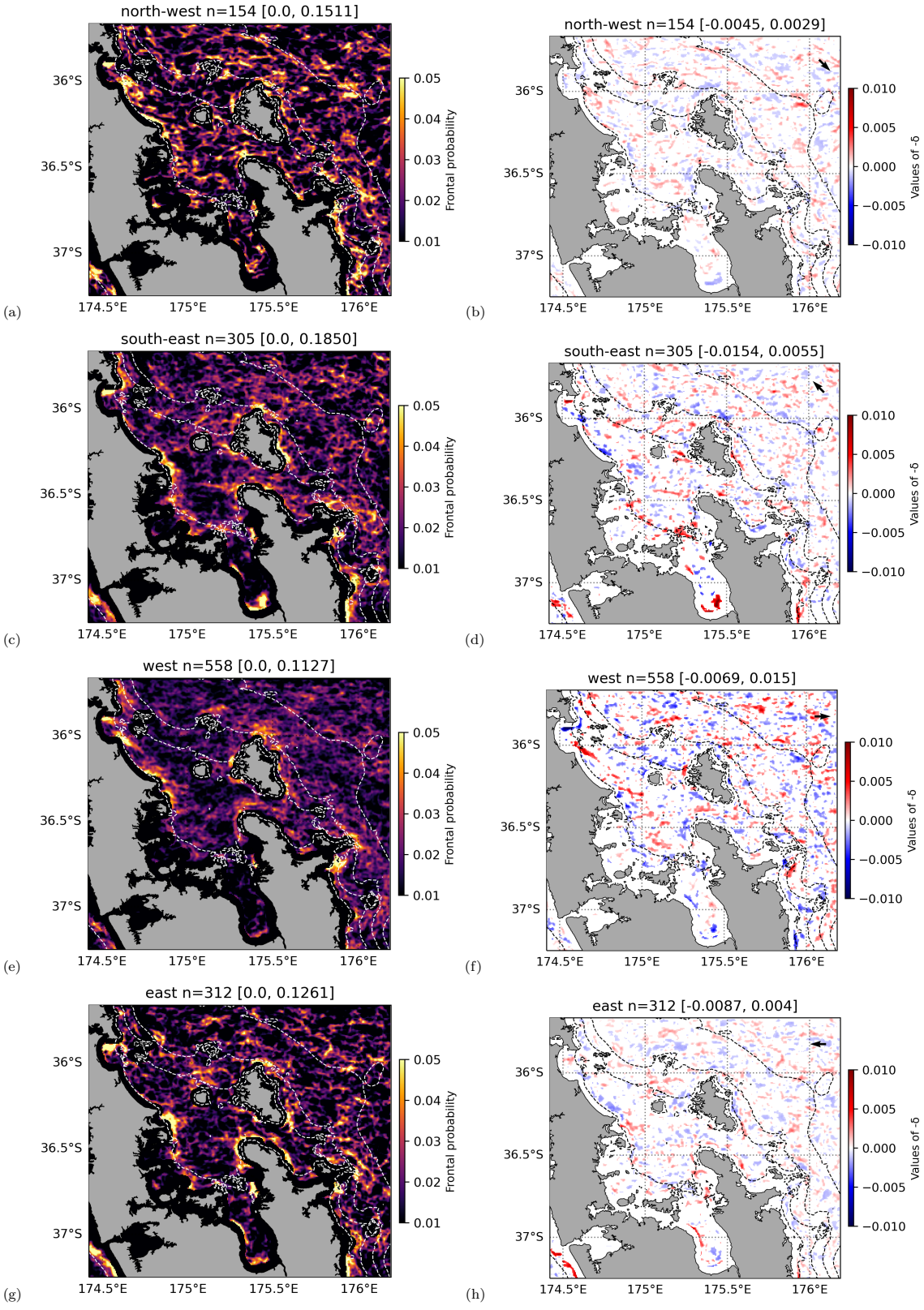

Figure 4. Probability maps and values of $-\delta$ outside of the 75^{th} percentile confidence interval based on wind orientation, top to bottom: North-West (a, b), South-East (c, d), West (e, f), East (g,h). Probabilities are on the left column (a, c, e, g) and δ on the right. Dashed line indicate 40, 70, 100 and 200m depth. The title of each sub-figure indicate the factor, n the number of days and the min and max values. Wind orientation arrow displayed in δ maps top-right corner.

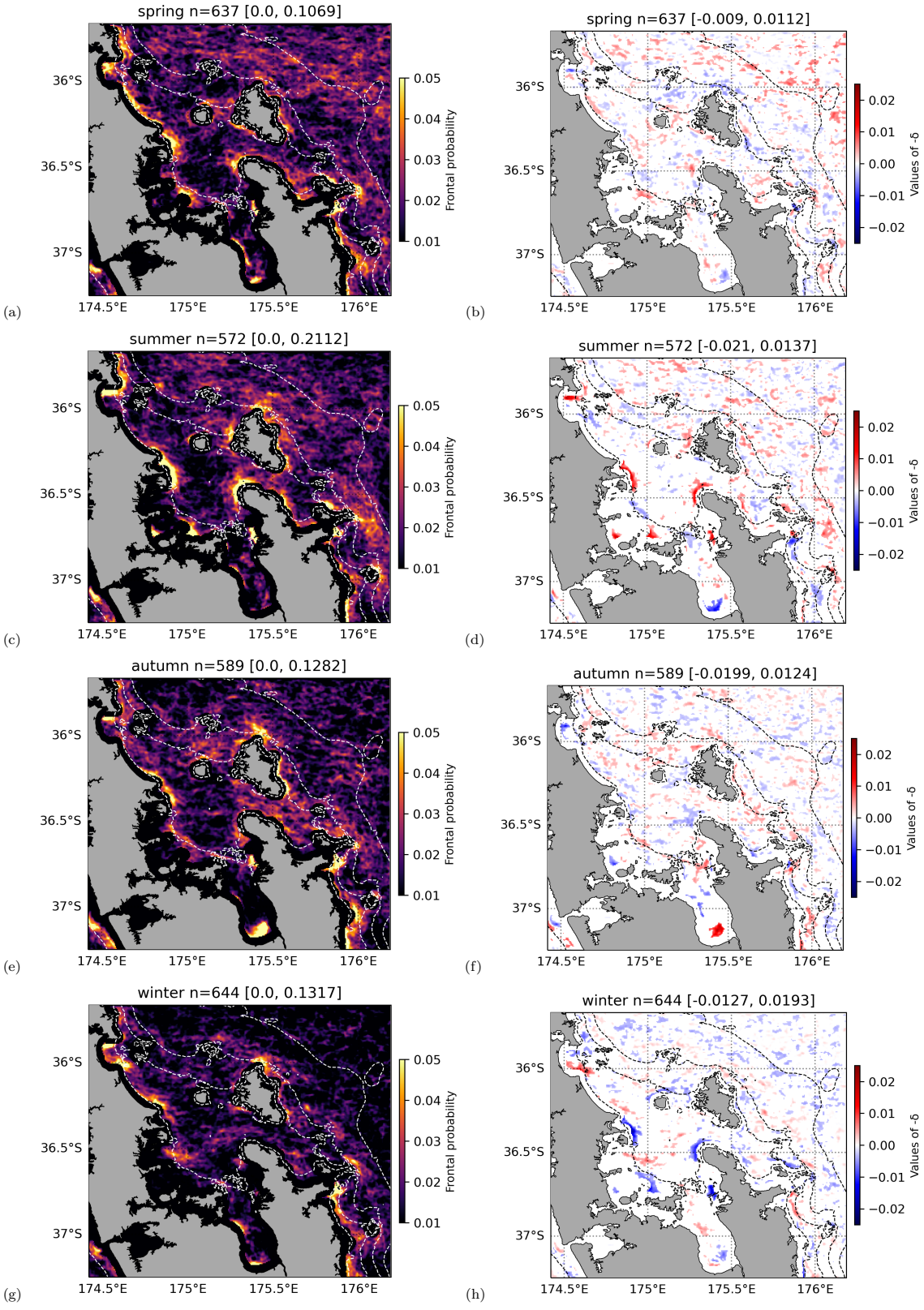

Figure 5. Probability maps and values of $-\delta$ outside of the 75^{th} percentile confidence interval during seasons, top to bottom: spring (a, b), summer (c, d), autumn (e, f), winter (g, h). Probabilities are on the left column (a, c, e, g) and δ on the right. Dashed line indicate 40, 70, 100 and 200m depth. The title of each sub-figure indicate the factor, n the number of days and the min and max values. Note the change of scale in δ.

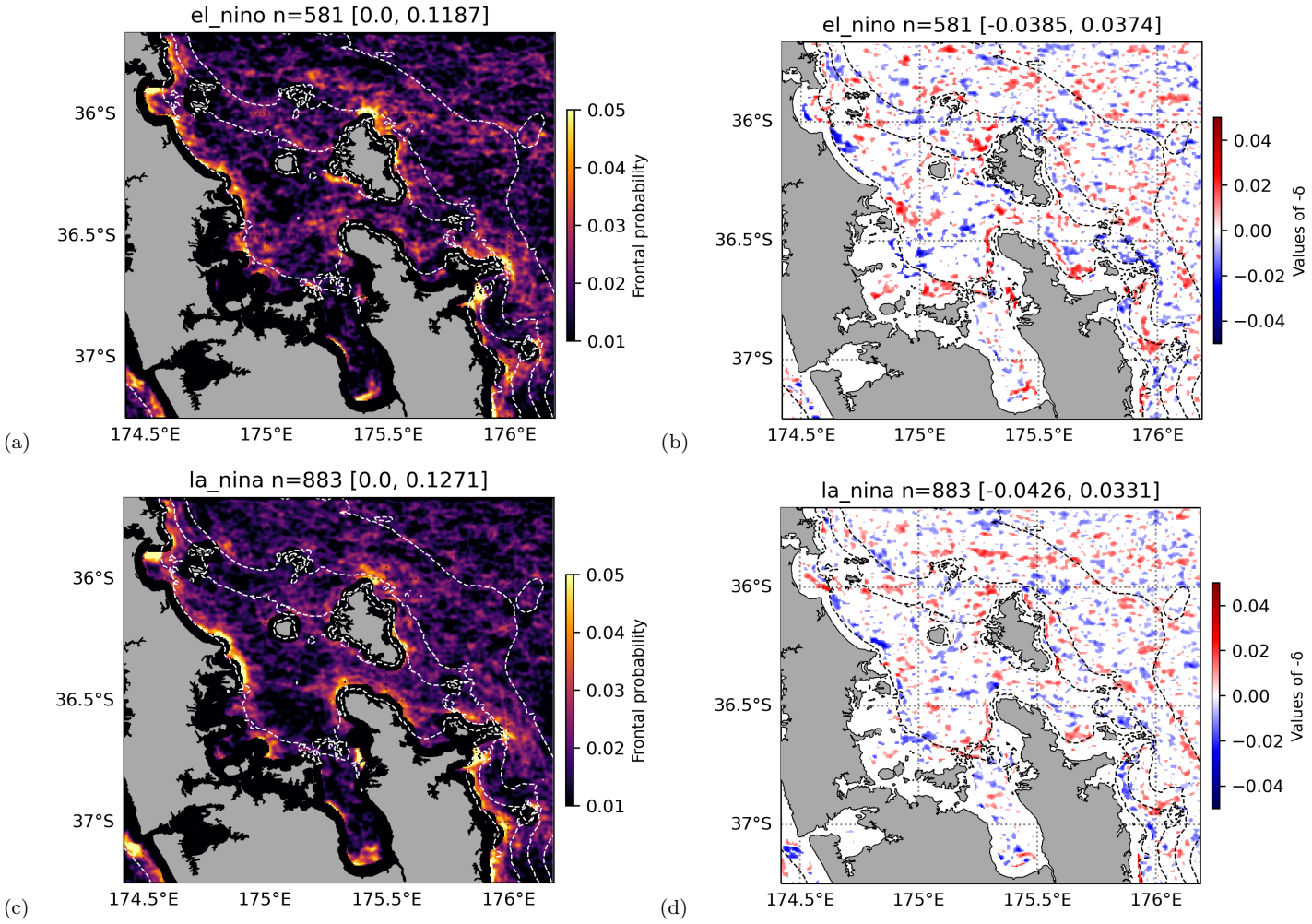

Figure 6. Probability maps and values of $-\delta$ outside of the 75^{th} percentile confidence interval during ENSO phases, top to bottom: *El Niño* (a, b), *La Niña* (c, d). Probabilities are on the left column (a, c) and δ on the right. Dashed line indicate 40, 70, 100 and 200m depth. The title of each sub-figure indicate the factor, n the number of days and the min and max values. Note the change of scale in δ.

4 Discussion

Frontal probabilities in Tīpaka Moana Te Moana Nui a Toi Hauraki Gulf (HG) are highest along the coast and in the middle of the outer-Gulf between Kawau, Waiheke and the Colville Cape (figure 3). Our results indicate that the distribution of fine-scale fronts is modulated by winds, season and ENSO phases. Our most important observations are:

- Fronts along the 40 and 70m isobath separate the Gulf in 3 segments.
- Most winds directions have a significant impact on the position of fronts, especially SW, West and East.
- Seasonal shifts of wind direction (east in summer-autumn, west in winter-spring) result in frontal movements across the Gulf
- The ENSO cycle changes the separation between the inner and outer Gulf, "closing" during *El Niño* and "opening" during *La Niña*

Across all studied parameters (wind, season, ENSO), fronts probability patches in HG overlap with the 70m and 40m isobath. The distribution of fronts tends to separate HG in three distinct sub-regions, being outer-Gulf, inner-Gulf, and Firth of Thames. More precisely, the Firth of Thames to inner Gulf separation is enforced by fronts following the 40m isobath, while fronts between Kawau and Cape Colville following the 70m isobath might inhibit the mixing of waters from the inner and outer gulf. This separation is accentuated during *El Niño* periods and attenuated during *La Niña*.

To correctly interpret the observe patterns, we need to account for the intricacies of using ocean colour. Isolating the sediment from chlorophyll is a key element of OLCI dataset processing, yet Blondeau-Patissier et al. (2014) showed that none of the current algorithms are able to properly remove the sediment signal, which will in turn impact the front detection results using OLCI. The only processing in removing the sediment signal was done prior to download by the OC4ME algorithm from Copernicus (EUMETSAT, 2021). We also removed values of CHL above 30mg.m^{-3}, considering that OC4ME tend to overestimate values above 30 (EUMETSAT, 2021). Hence, it is likely that at least some of the coastal fronts results from gradients in sediment concentration (for example, associated with increase rainfall and river outflows) rather that gradients in chlorophyll, especially in the Firth of Thames (O'Callaghan & Stevens, 2017). However, these regions highlighted at hotspots of frontal activities, would still represent regions where water masses of different optical properties converge. If in one of the sides of the front the ocean colour signal is heavily dominated by sediments, we expect that the waters therein would likely have very different biological properties compared to the clearer waters brought nearby by the frontal circulation, even if this difference is not measured in terms of chlorophyll. Very high values of probability directly next to the shore are due to the sensibility of the algorithm which enables us to detect fronts in the highly dynamic coastal environment.

Because of our work hypothesis being that biologically important fronts are characterised by strong chlorophyll gradient as depicted by Lévy et al. (2018), we chose to use a gradient-based front detection algorithm as the core calculation of the pyBOA. The original BOA was developed by Belkin and O'Reilly (2009), and later used by Lin et al. (2019) and Galuardi (2012), precisely to deal with strong chlorophyll gradients created by the *slope-shelf* effect (Belkin & O'Reilly, 2009). The presence of the shelf and slope nearby highly influence the circulation in HG (Stevens et al., 2021; Zeldis et al., 2004). Our results are consistent with this view showing an overlap of fronts with the 100m isobath, in addition to others more related to the bathymetry than the shelf (40, 70m). This shelf effect is documented in other parts of Aotearoa New Zealand such as around the Otago shelf (Hopkins et al., 2010).

The frontal probabilities movements also relate to changes in wind direction throughout the seasons, with westerlies in winter and spring, switching to easterlies in summer and autumn. This cycle explain the nearshore-offshore oscillation seen in figure 5 and are also related to phyto and zooplankton changes (Chang et al., 2003; Jillett, 1971; Sharples, 1997). The oscillation observed in HG are similar to the observation of Hopkins et al. (2010), showing the South Tropical Front close to shore in summer-autumn and further offshore during winter-spring. This similarity in behavior may originate from the similarity of bathymetry, both areas having strong shelf break (Hopkins et al., 2010; Zeldis et al., 2004). In addition, the switch to easterlies in *La Niña* periods (Zeldis et al., 2004) explains why some of the fronts observed seems pushed into the Gulf by comparison to *Neutral* ENSO phase.

The effect of tides on the movement of fronts are not studied in this article. However, this study by Hu et al. (2016) suggests that tides are important factor in fine-scale structure movement, sometimes moving sediment fronts up to 10 km based on the current. While this approach was not feasible here due to data availability (one image per day), we suspect the tides have potentially shift the position of fronts across the Gulf. Multiple images throughout the day on a similar resolution would allow future description of the tidal effect in our study area.

Fronts are associated with enhanced productivity (Lévy et al., 2018; McGillicuddy, 2016) regardless of the scale considered. This boosted productivity and altered conditions are important feeding grounds used by megafauna (Braun et al., 2019; Snyder et al., 2017) and the fishing industry alike (Watson et al., 2018). Spatial shifts in frontal distribution associated to changes in seasons may therefore displace hotspots of productivity across the HG, potentially driving the movement of aggregations of seabirds (Gaskin, 2021) or overwintering cetaceans (Gostischa et al., 2021; Izadi et al., 2022). In addition, seasonal variations of frontal locations can impact the dispersal of planktonic larvae from sessile species with different spawning times (Michie, 2023). For example, crayfish mating period in winter (Kelly, 2001; MacDiarmid, 1989) matches with increase frontal probability in the inner Gulf contributing to their dispersion or retention.

On a larger scale, looking at the effect of the ENSO phases, it appears that the shift from one phase to another (*e.g. El Niño* to *La Niña*) has major impact of seabirds (Gaskin, 2021). The most notable effect observed by Gaskin (2021) was a drop in birds weight after each shift from *El Niño* to *La Niña*. This is hypothesized to be linked with shifts in their zooplanktonic and fish prey quality and distribution. Spatial shifts in frontal distribution might be a potential driver of the distribution of prey items for local megafauna.

5 Conclusion

This study compiled a first map of frontal probabilities for the HG by improving an existing algorithm in order to detect fine-scale fronts from OLCI. We successfully used a gradient approach to reliably identify fronts and characterise the frontal patterns both spatially and temporally. We show that the fronts in HG follow specific seasonal and ENSO patterns, governed by the bathymetry and winds. In addition, the segmentation of the Gulf in 3 different sub-basins is proven coherent from a frontal perspective.

Acronyms

BOA Belkin and O'Reilly Algorithm
CHL Chlorophyll-a
EAuC East Auckland Current
ENSO El Niño Southern Oscillation
OLCI Ocean-Land Color Instrument

SOI Southern Oscillation Index
HG Tīpaka Moana Te Moana Nui a Toi Hauraki Gulf

6 Open Research

The wind data used in this article were provided by Meteorological Service of New Zealand Ltd, covering the stations of Mokohinau. The satellite data used for the detection are provided by Copernicus Marine Services (Copernicus, 2016). All maps presented here made using python 3.9 package *cartopy* (Met Office, 2010 - 2015). The pyBOA 1.0.0 is freely available: `https://doi.org/10.5281/zenodo.8135921`. This version of the algorithm was build using python 3.9 with Anaconda3 2022.05.

Acknowledgments
Our thanks go to Dr. Igor Belkin, Dr. Lei Lin and Dr. Benjamin Galuardi for answering our questions about transferring the code to python and providing their own code in MATLAB/R-core. Our thanks as well to the statistical services to the University of Auckland for their advice and review of the methods.

We thank Pr. Andrew Jeffs for supporting this project. This work was supported by the University of Auckland via the Faculty Research Development Fund (Grant 3724591) and the Departmental Performance Based Research Funding (PBRF).

References

Barkley, R. (1970). The kuroshio current.

Belkin, I. M., & O'Reilly, J. E. (2009, October). An algorithm for oceanic front detection in chlorophyll and SST satellite imagery. *Journal of Marine Systems*, *78*(3), 319–326. Retrieved 2021-11-16, from `https://www.sciencedirect.com/science/article/pii/S0924796309000682` doi: 10.1016/j.jmarsys.2008.11.018

Blondeau-Patissier, D., Gower, J. F. R., Dekker, A. G., Phinn, S. R., & Brando, V. E. (2014, April). A review of ocean color remote sensing methods and statistical techniques for the detection, mapping and analysis of phytoplankton blooms in coastal and open oceans. *Progress in Oceanography*, *123*, 123–144. Retrieved 2022-12-07, from `https://www.sciencedirect.com/science/article/pii/S0079661114000020` doi: 10.1016/j.pocean.2013.12.008

Braun, C. D., Gaube, P., Sinclair-Taylor, T. H., Skomal, G. B., & Thorrold, S. R. (2019, August). Mesoscale eddies release pelagic sharks from thermal constraints to foraging in the ocean twilight zone. *Proceedings of the National Academy of Sciences*, *116*(35), 17187–17192. Retrieved 2022-06-26, from `https://www.pnas.org/doi/10.1073/pnas.1903067116` (Publisher: Proceedings of the National Academy of Sciences) doi: 10.1073/pnas.1903067116

Cayula, J.-F., & Cornillon, P. (1992, February). Edge Detection Algorithm for SST Images. *Journal of Atmospheric and Oceanic Technology*, *9*(1), 67–80. Retrieved 2021-11-23, from `https://journals.ametsoc.org/view/journals/atot/9/1/1520-0426_1992_009_0067_edafsi_2_0_co_2.xml` (Publisher: American Meteorological Society Section: Journal of Atmospheric and Oceanic Technology) doi: 10.1175/1520-0426(1992)009⟨0067:EDAFSI⟩2.0.CO;2

Chang, F. H., Zeldis, J., Gall, M., & Hall, J. (2003, July). Seasonal and spatial variation of phytoplankton assemblages, biomass and cell size from spring to summer across the north-eastern New Zealand continental shelf. *Journal of Plankton Research*, *25*(7), 737–758. Retrieved 2021-12-03, from `https://doi.org/10.1093/plankt/25.7.737` doi: 10.1093/plankt/25.7.737

Colella, S., Böhm, E., Cesarini, C., Garnesson, P., Netting, J., & Calton,

B. (2022, February). *PRODUCT USER MANUAL For Ocean Colour Products OCEANCOLOUR_glo_bgc_l3_nrt_009_101 OCEANCOLOUR_glo_bgc_l4_nrt_009_102 OCEANCOLOUR_glo_bgc_l3_my_009_103 OCEANCOLOUR_glo_bgc_l4_my_009_104 OCEANCOLOUR_glo_bgc_l3_my_009_107 OCEANCOLOUR_glo_bgc_l4_my_009_108 OCEANCOLOUR_atl_bgc_l3_nrt_009_111 OCEANCOLOUR_atl_bgc_l4_nrt_009_112 OCEANCOLOUR_atl_bgc_l3_my_009_113 OCEANCOLOUR_atl_bgc_l4_my_009_114 OCEANCOLOUR_atl_bgc_l4_nrt_009_116 OCEANCOLOUR_atl_bgc_l4_my_009_118 OCEANCOLOUR_arc_bgc_l3_nrt_009_121 OCEANCOLOUR_arc_bgc_l4_nrt_009_122 OCEANCOLOUR_arc_bgc_l3_nrt_009_123 OCEANCOLOUR_arc_bgc_l4_nrt_009_124 OCEANCOLOUR_bal_bgc_l3_nrt_009_131 OCEANCOLOUR_bal_bgc_l4_nrt_009_132 OCEANCOLOUR_bal_bgc_l3_my_009_133 OCEANCOLOUR_med_bgc_l3_nrt_009_141 OCEANCOLOUR_med_bgc_l4_nrt_009_142 OCEANCOLOUR_med_bgc_l3_my_009_143 OCEANCOLOUR_med_bgc_l4_my_009_144 OCEANCOLOUR_blk_bgc_l3_nrt_009_151 OCEANCOLOUR_blk_bgc_l4_nrt_009_152 OCEANCOLOUR_blk_bgc_l3_my_009_153 OCEANCOLOUR_blk_bgc_l4_my_009_154 Issue: 1.0* (Tech. Rep.). European Organisation for the Exploitation of Meteorological Satellites. Retrieved 2022-08-02, from https://catalogue.marine.copernicus.eu/documents/PUM/CMEMS-OC-PUM.pdf

Copernicus. (2016, May). *Global Ocean Colour (Copernicus-GlobColour), Bio-Geo-Chemical, L3 (daily) from Satellite Observations (1997-ongoing).* Retrieved 2022-01-01, from https://doi.org/10.48670/moi-00280

Council, A. (2021). *The hapū and iwi of Tāmaki Makaurau.* Retrieved 2021-11-02, from http://www.aucklandcouncil.govt.nz/plans-projects-policies-reports-bylaws/our-plans-strategies/auckland-plan/about-the-auckland-plan/Pages/iwi-tamaki-makaurau.aspx

Cowles, T., Desiderio, R., & Carr, M.-E. (1998). Small-Scale Planktonic Structure: Persistence and Trophic Consequences. *Oceanography*, *11*(1), 4–9. Retrieved 2021-11-18, from https://tos.org/oceanography/article/small-scale-planktonic-structure-persistence-and-trophicconsequences doi: 10.5670/oceanog.1998.08

EUMETSAT. (2021, February). *Sentinel-3 Product Notice – OLCI Level-2 Ocean Colour* (Tech. Rep.). European Organisation for the Exploitation of Meteorological Satellites. Retrieved 2022-12-12, from https://www-cdn.eumetsat.int/files/2021-02/S3%20PN-OLCI-L2M_003_00%20-%20Sentinel-3%20Product%20Notice%20%E2%80%93%20OLCI%20Level-2%20Ocean%20Colour.pdf

Galuardi, B. (2012, January). *boaR-package: The Belkin-O'Reilly front detection algorithm.* Retrieved 2022-07-14, from https://rdrr.io/github/galuardi/boaR/man/boaR-package.html

Gaskin, C. (2021). *State of our Seabirds 2021 - Seabird ecology, research and conservation for the wider Hauraki Gulf / Tīkapa Moana / Te Moananui-ā-Toi region* (Tech. Rep.). Auckland, New Zealand: Northern New Zealand Seabirds Charitable Trust.

Gostischa, J., Massolo, A., & Constantine, R. (2021). Multi-Species Feeding Association Dynamics Driven by a Large Generalist Predator. *Frontiers in Marine Science*, *8*. Retrieved 2023-04-24, from https://www.frontiersin.org/articles/10.3389/fmars.2021.739894

Hopkins, J., Shaw, A., & Challenor, P. (2010, August). The Southland Front, New Zealand: Variability and ENSO correlations. *Continental Shelf Research*, *30*(14), 1535–1548. Retrieved 2023-07-10, from https://linkinghub.elsevier.com/retrieve/pii/S0278434310001937 doi:

10.1016/j.csr.2010.05.016

Hu, Z., Pan, D., He, X., & Bai, Y. (2016, February). Diurnal Variability of Turbidity Fronts Observed by Geostationary Satellite Ocean Color Remote Sensing. *Remote Sensing*, *8*(2), 147. Retrieved 2023-08-15, from https://www.mdpi.com/2072-4292/8/2/147 (Number: 2 Publisher: Multidisciplinary Digital Publishing Institute) doi: 10.3390/rs8020147

Izadi, S., Aguilar de Soto, N., Constantine, R., & Johnson, M. (2022). Feeding tactics of resident Bryde's whales in New Zealand. *Marine Mammal Science*, *38*(3), 1104–1117. Retrieved 2023-04-24, from https://onlinelibrary.wiley.com/doi/abs/10.1111/mms.12918 (_eprint: https://onlinelibrary.wiley.com/doi/pdf/10.1111/mms.12918) doi: 10.1111/mms.12918

Jillett, J. B. (1971). *Zooplankton and hydrology of Hauraki Gulf, New Zealand*. Retrieved 2022-02-21, from http://archive.org/details/nzoimemoir00531971

Kelly, S. (2001). Temporal variation in the movement of the spiny lobster Jasus edwardsii. *Marine and Freshwater Research*, *52*(3), 323. Retrieved 2023-07-11, from http://www.publish.csiro.au/?paper=MF00028 doi: 10.1071/MF00028

Lehahn, Y., d'Ovidio, F., Lévy, M., & Heifetz, E. (2007). Stirring of the northeast Atlantic spring bloom: A Lagrangian analysis based on multisatellite data. *Journal of Geophysical Research: Oceans*, *112*(C8). Retrieved 2022-06-16, from https://onlinelibrary.wiley.com/doi/abs/10.1029/2006JC003927 (_eprint: https://onlinelibrary.wiley.com/doi/pdf/10.1029/2006JC003927) doi: 10.1029/2006JC003927

Levine, R. S., Yorita, K. L., Walsh, M. C., & Reynolds, M. G. (2009, January). A method for statistically comparing spatial distribution maps. *International Journal of Health Geographics*, *8*(1), 7. Retrieved 2022-08-07, from https://doi.org/10.1186/1476-072X-8-7 doi: 10.1186/1476-072X-8-7

Lin, L., Liu, D., Luo, C., & Xie, L. (2019, March). Double fronts in the Yellow Sea in summertime identified using sea surface temperature data of multi-scale ultra-high resolution analysis. *Continental Shelf Research*, *175*, 76–86. Retrieved 2022-07-26, from https://linkinghub.elsevier.com/retrieve/pii/S0278434318302802 doi: 10.1016/j.csr.2019.02.004

Liu, X., & Levine, N. M. (2016, February). Enhancement of phytoplankton chlorophyll by submesoscale frontal dynamics in the North Pacific Subtropical Gyre. *Geophysical Research Letters*, *43*(4), 1651–1659. Retrieved 2021-12-15, from https://onlinelibrary.wiley.com/doi/10.1002/2015GL066996 doi: 10.1002/2015GL066996

Lévy, M., Ferrari, R., Franks, P. J. S., Martin, A. P., & Rivière, P. (2012). Bringing physics to life at the submesoscale. *Geophysical Research Letters*, *39*(14). Retrieved 2022-08-02, from https://onlinelibrary.wiley.com/doi/abs/10.1029/2012GL052756 (_eprint: https://onlinelibrary.wiley.com/doi/pdf/10.1029/2012GL052756) doi: 10.1029/2012GL052756

Lévy, M., Franks, P. J. S., & Smith, K. S. (2018, November). The role of submesoscale currents in structuring marine ecosystems. *Nature Communications*, *9*(1), 4758. Retrieved 2021-11-18, from https://www.nature.com/articles/s41467-018-07059-3/ (Bandiera_abtest: a Cc_license_type: cc_by Cg_type: Nature Research Journals Number: 1 Primary_atype: Reviews Publisher: Nature Publishing Group Subject_term: Marine biology;Ocean sciences Subject_term_id: marine-biology;ocean-sciences) doi: 10.1038/s41467-018-07059-3

MacDiarmid, A. B. (1989). Moulting and reproduction of the spiny lobster Jasus edwardsii (Decapoda: Palinuridae) in northern New Zealand. *Marine Biology*, *103*(3), 303–310. Retrieved 2023-07-11, from http://link.springer.com/10

.1007/BF00397263 doi: 10.1007/BF00397263

Mahadevan, A. (2016). The Impact of Submesoscale Physics on Primary Productivity of Plankton. *Annual Review of Marine Science*, *8*(1), 161–184. Retrieved 2021-11-18, from https://doi.org/10.1146/annurev-marine-010814-015912 (_eprint: https://doi.org/10.1146/annurev-marine-010814-015912) doi: 10.1146/annurev-marine-010814-015912

Mangolte, I., Lévy, M., Haëck, C., & Ohman, M. D. (2023, March). *Sub-frontal niches of plankton communities driven by transport and trophic interactions at ocean fronts* (preprint). Biogeophysics: Physical - Biological Coupling. Retrieved 2023-04-03, from https://egusphere.copernicus.org/preprints/2023/egusphere-2023-471/ doi: 10.5194/egusphere-2023-471

Mauzole, Y., Torres, H., & Fu, L. (2020, February). Patterns and Dynamics of SST Fronts in the California Current System. *Journal of Geophysical Research: Oceans*, *125*. doi: 10.1029/2019JC015499

McGillicuddy, D. J. (2016). Mechanisms of Physical-Biological-Biogeochemical Interaction at the Oceanic Mesoscale. *Annual Review of Marine Science*, *8*(1), 125–159. Retrieved 2021-11-18, from https://doi.org/10.1146/annurev-marine-010814-015606 (_eprint: https://doi.org/10.1146/annurev-marine-010814-015606) doi: 10.1146/annurev-marine-010814-015606

Met Office. (2010 - 2015). Cartopy: a cartographic python library with a matplotlib interface [Computer software manual]. Exeter, Devon. Retrieved from https://scitools.org.uk/cartopy

Michie, C. A. G. (2023). *Variation in larval dispersal patterns and its power in predicting genetic divergence of benthic marine invertebrates around new zealand* (Unpublished doctoral dissertation). ResearchSpace@ Auckland.

Miller, P. (2004, April). Multi-spectral front maps for automatic detection of ocean colour features from SeaWiFS. *International Journal of Remote Sensing*, *25*(7-8), 1437–1442. Retrieved 2022-05-19, from https://doi.org/10.1080/01431160310001592409 (Publisher: Taylor & Francis _eprint: https://doi.org/10.1080/01431160310001592409) doi: 10.1080/01431160310001592409

NOAA. (2022). *SOI indices 1951-current time.* Retrieved 2022-08-26, from https://www.cpc.ncep.noaa.gov/data/indices/soi

O'Callaghan, J. M., & Stevens, C. L. (2017). Evaluating the Surface Response of Discharge Events in a New Zealand Gulf-ROFI. *Frontiers in Marine Science*, *4*. Retrieved 2022-10-06, from https://www.frontiersin.org/articles/10.3389/fmars.2017.00232

Palter, J. B. (2015). The Role of the Gulf Stream in European Climate. *Annual Review of Marine Science*, *7*(1), 113–137. Retrieved 2020-11-03, from https://doi.org/10.1146/annurev-marine-010814-015656 (_eprint: https://doi.org/10.1146/annurev-marine-010814-015656) doi: 10.1146/annurev-marine-010814-015656

Ridgway, K., & Hill, K. (2009). The East Australian current. In E. S. Poloczanska, A. J. Hobday, & A. J. Richardson (Eds.), . NCCARF Publication. Retrieved 2022-07-26, from https://nora.nerc.ac.uk/id/eprint/528665/

Sharples, J. (1997, June). Cross-shelf intrusion of subtropical water into the coastal zone of northeast New Zealand. *Continental Shelf Research*, *17*(7), 835–857. Retrieved 2021-07-07, from https://linkinghub.elsevier.com/retrieve/pii/S027843439600060X doi: 10.1016/S0278-4343(96)00060-X

Smith, W. L., Rao, P. K., Koffler, R., & Curtis, W. R. (1970, August). The determination of sea-surface temperature from satellite high resolution infrared window ratiation measurements. *Monthly Weather Review*, *98*(8), 604–611. Retrieved 2023-07-11, from https://journals.ametsoc.org/view/journals/mwre/98/8/1520-0493_1970_098_0604_tdosst_2_3_co_2.xml (Publisher: American Meteorological Society Section: Monthly Weather Review) doi:

10.1175/1520-0493(1970)098⟨0604:TDOSST⟩2.3.CO;2

Snyder, S., Franks, P. J. S., Talley, L. D., Xu, Y., & Kohin, S. (2017). Crossing the line: Tunas actively exploit submesoscale fronts to enhance foraging success. *Limnology and Oceanography Letters*, *2*(5), 187–194. Retrieved 2022-05-26, from https://onlinelibrary.wiley.com/doi/abs/10.1002/lol2.10049 (_eprint: https://onlinelibrary.wiley.com/doi/pdf/10.1002/lol2.10049) doi: 10.1002/lol2.10049

Stevens, C. L., O'Callaghan, J. M., Chiswell, S. M., & Hadfield, M. G. (2021, January). Physical oceanography of New Zealand/Aotearoa shelf seas – a review. *New Zealand Journal of Marine and Freshwater Research*, *55*(1), 6–45. Retrieved 2022-01-03, from https://doi.org/10.1080/00288330.2019.1588746 (Publisher: Taylor & Francis _eprint: https://doi.org/10.1080/00288330.2019.1588746) doi: 10.1080/00288330.2019.1588746

Thomas, L. N., Tandon, A., & Mahadevan, A. (2008). Submesoscale processes and dynamics. In M. W. Hecht & H. Hasumi (Eds.), *Geophysical Monograph Series* (Vol. 177, pp. 17–38). Washington, D. C.: American Geophysical Union. Retrieved 2022-01-26, from https://onlinelibrary.wiley.com/doi/10.1029/177GM04 doi: 10.1029/177GM04

Watson, J. R., Fuller, E. C., Castruccio, F. S., & Samhouri, J. F. (2018). Fishermen Follow Fine-Scale Physical Ocean Features for Finance. *Frontiers in Marine Science*, *5*. Retrieved 2022-04-19, from https://www.frontiersin.org/article/10.3389/fmars.2018.00046

Zeldis, J. R., Walters, R. A., Greig, M. J. N., & Image, K. (2004, March). Circulation over the northeastern New Zealand continental slope, shelf and adjacent Hauraki Gulf, during spring and summer. *Continental Shelf Research*, *24*(4), 543–561. Retrieved 2022-12-08, from https://www.sciencedirect.com/science/article/pii/S0278434303002449 doi: 10.1016/j.csr.2003.11.007

Zeldis, J. R., & Willis, K. (2015, January). Biogeographic and trophic drivers of mesozooplankton distribution on the northeast continental shelf and in Hauraki Gulf, New Zealand. *New Zealand Journal of Marine and Freshwater Research*, *49*(1), 69–86. Retrieved 2021-11-16, from https://doi.org/10.1080/00288330.2014.955806 (Publisher: Taylor & Francis _eprint: https://doi.org/10.1080/00288330.2014.955806) doi: 10.1080/00288330.2014.955806

Figure 1.

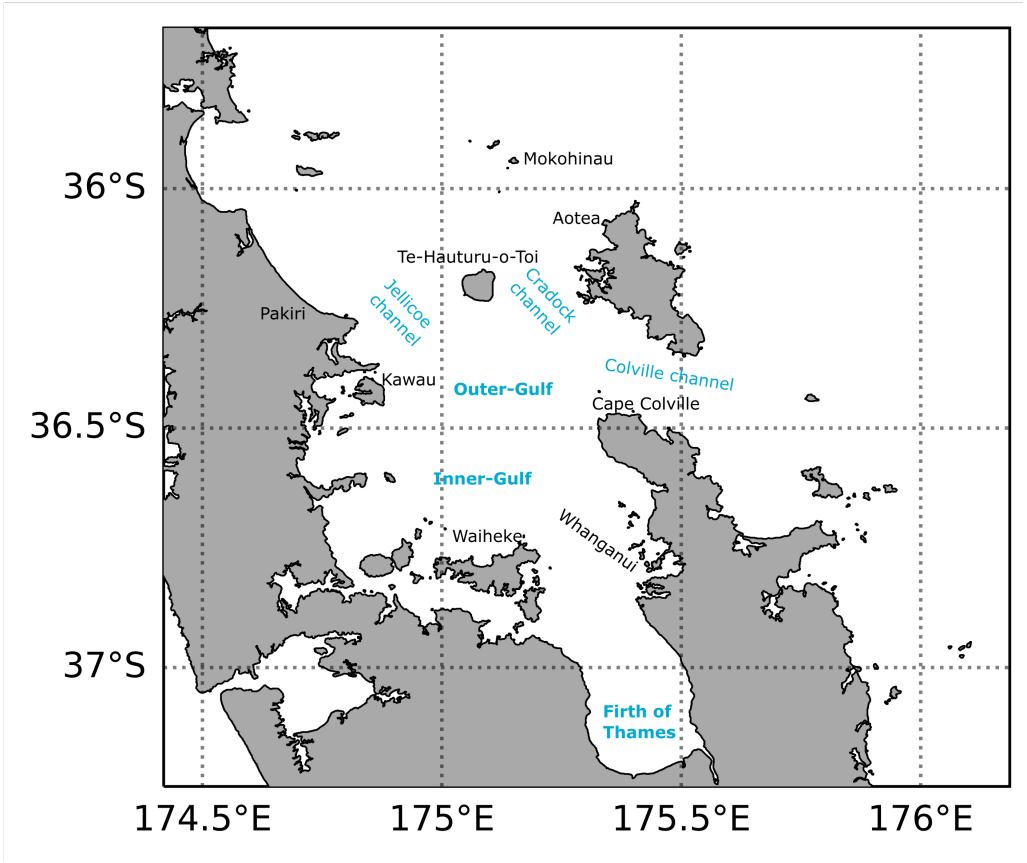
36°S
36.5°S
37°S
174.5°E
175°E
175.5°E
176°E
Mokohinau
Aotea
Te-Hauturu-o-Toi
Jellicoe channel
Cradock channel
Pakiri
Kawau
Outer-Gulf
Colville channel
Cape Colville
Inner-Gulf
Waiheke
Whanganui
Firth of Thames

Figure 2.

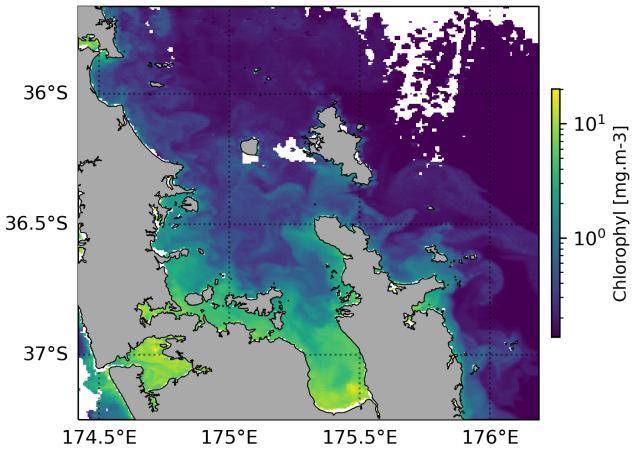

(a) Raw CHL from (Copernicus, 2016)

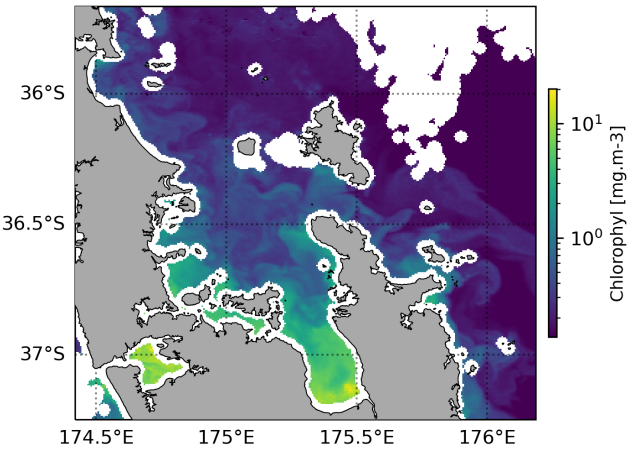

(b) Land and cloud proximity exclusion

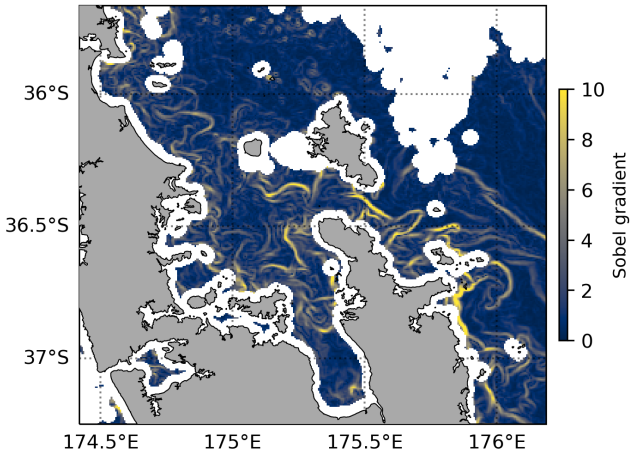

(c) Sobel gradient

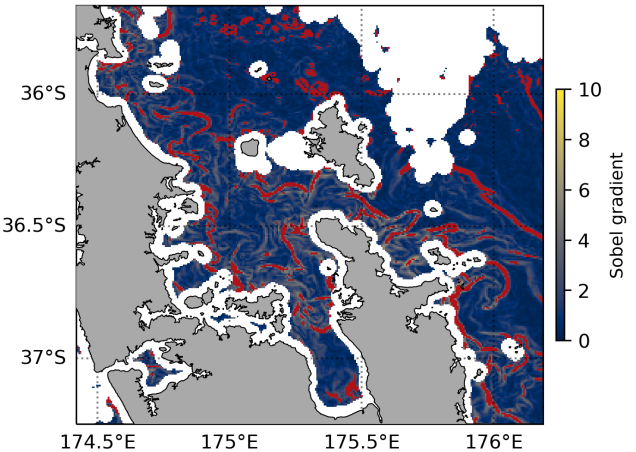

(d) Selected front areas in red

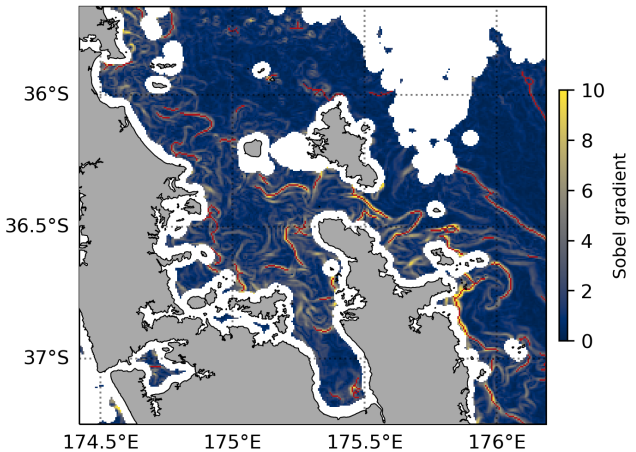

(e) Morphological thining to lines

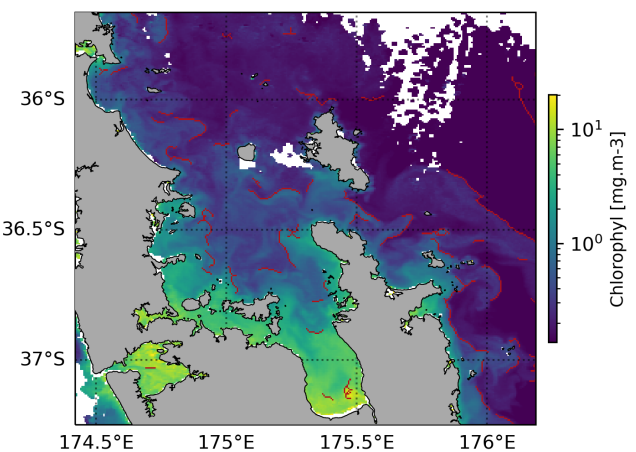

(f) Overlap of the front lines with the CHL

Figure 3.

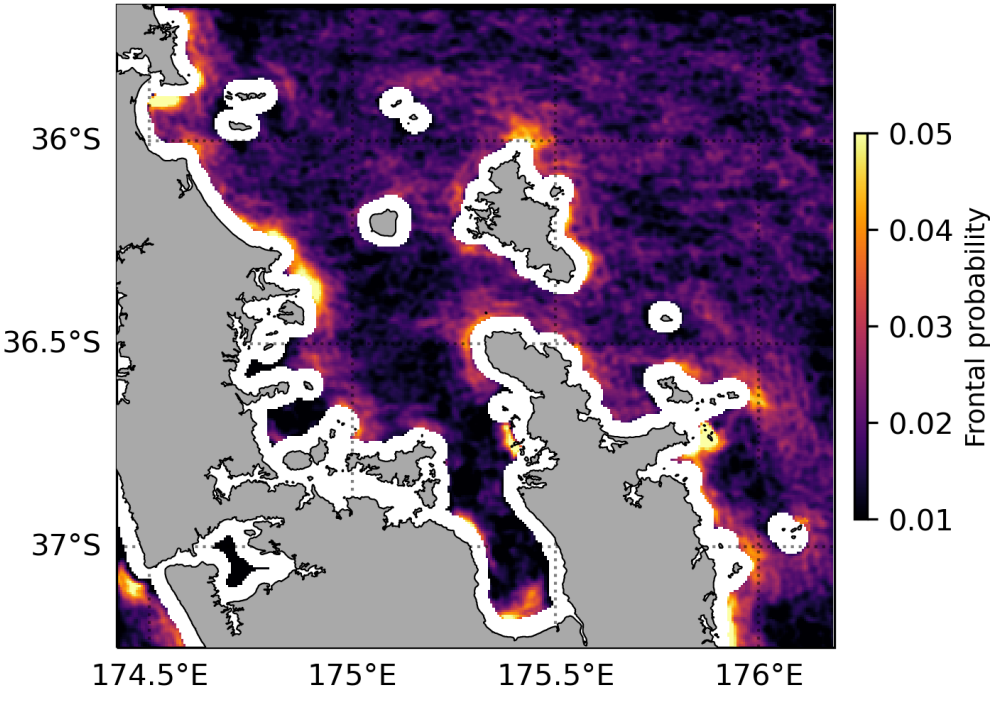
36°S
36.5°S
37°S
174.5°E
175°E
175.5°E
176°E
0.05
0.04
0.03
0.02
0.01
Frontal probability

Figure 4.

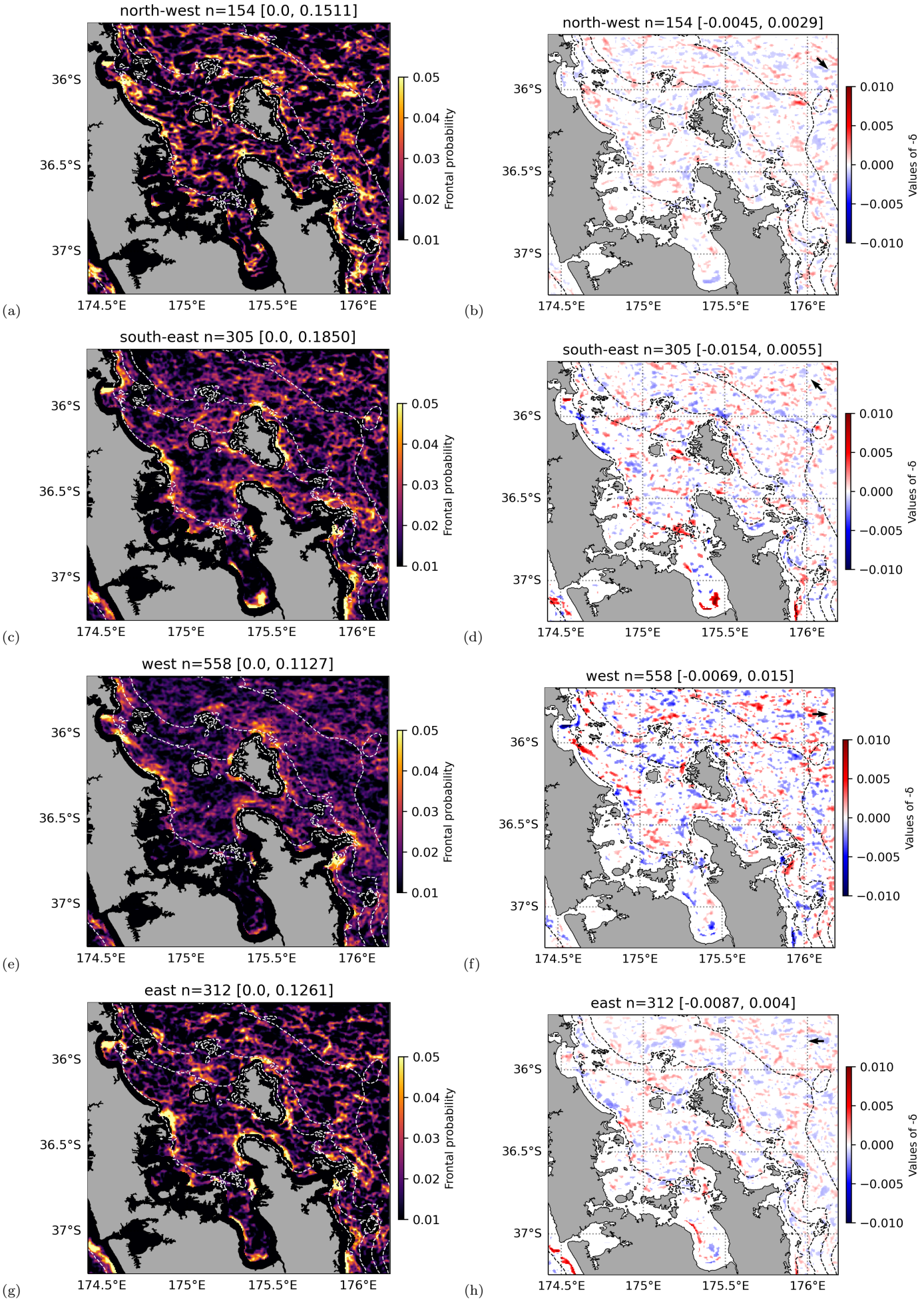
north-west n=154 [0.0, 0.1511]
north-west n=154 [-0.0045, 0.0029]
south-east n=305 [0.0, 0.1850]
south-east n=305 [-0.0154, 0.0055]
west n=558 [0.0, 0.1127]
west n=558 [-0.0069, 0.015]
east n=312 [0.0, 0.1261]
east n=312 [-0.0087, 0.004]
36°S
36.5°S
37°S
174.5°E
175°E
175.5°E
176°E
Frontal probability
Values of -δ
0.05
0.04
0.03
0.02
0.01
0.010
0.005
0.000
−0.005
−0.010
(a)
(b)
(c)
(d)
(e)
(f)
(g)
(h)

Figure 5.

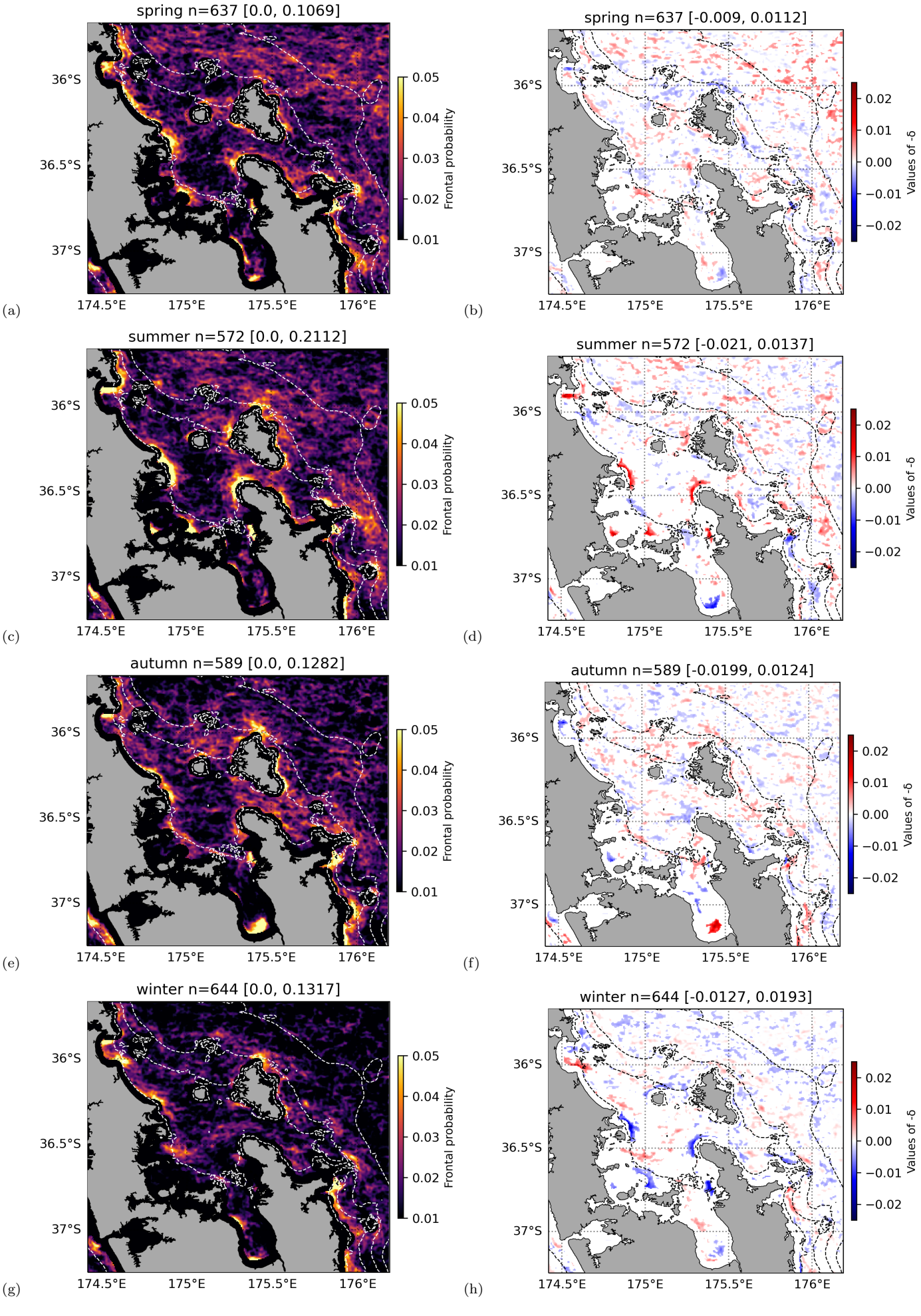
spring n=637 [0.0, 0.1069]
spring n=637 [-0.009, 0.0112]
summer n=572 [0.0, 0.2112]
summer n=572 [-0.021, 0.0137]
autumn n=589 [0.0, 0.1282]
autumn n=589 [-0.0199, 0.0124]
winter n=644 [0.0, 0.1317]
winter n=644 [-0.0127, 0.0193]
36°S
36.5°S
37°S
174.5°E
175°E
175.5°E
176°E
Frontal probability
0.05
0.04
0.03
0.02
0.01
Values of -δ
0.02
0.01
0.00
−0.01
−0.02
(a)
(b)
(c)
(d)
(e)
(f)
(g)
(h)

Figure 6.

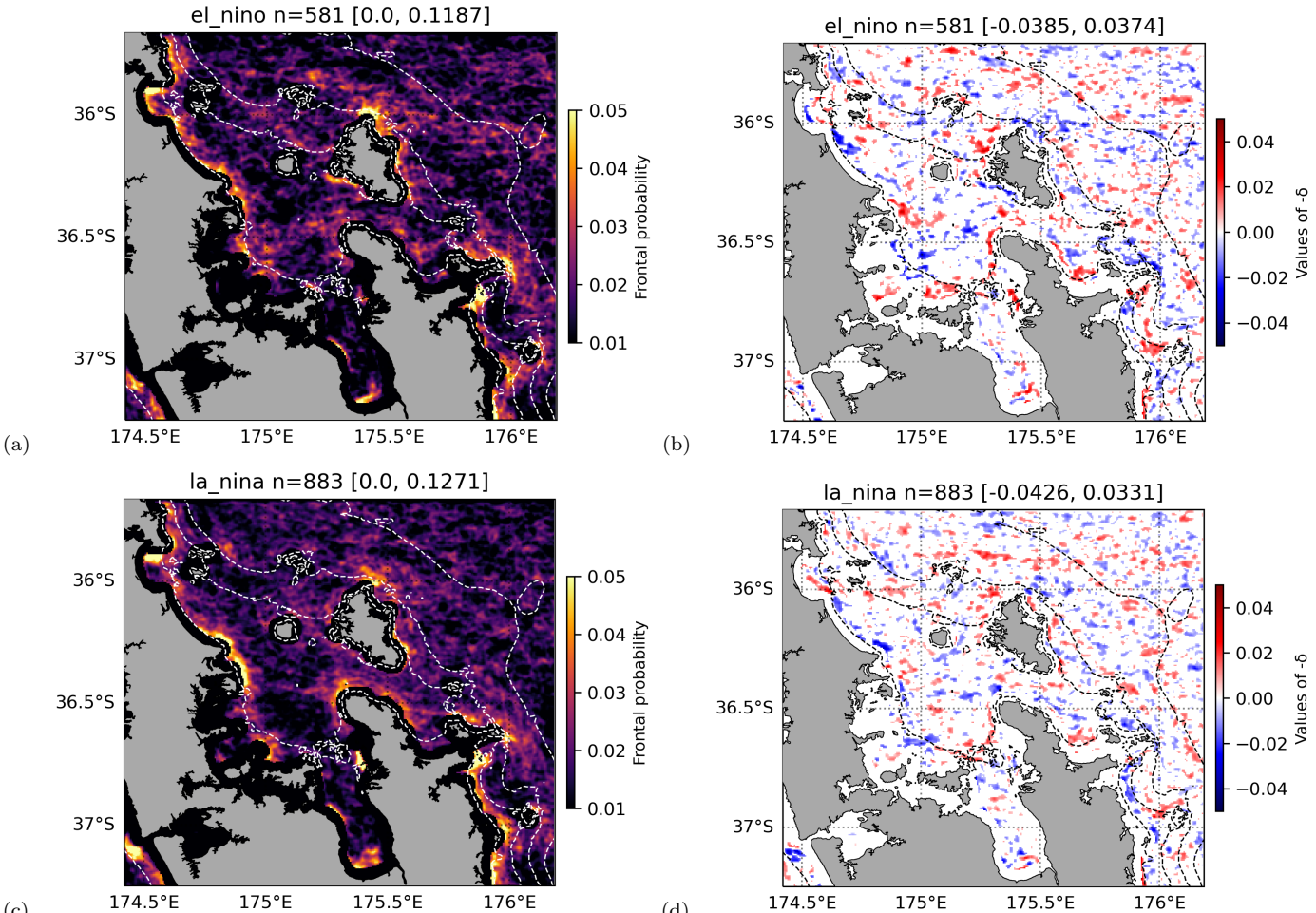
el_nino n=581 [0.0, 0.1187]
36°S
36.5°S
37°S
174.5°E
175°E
175.5°E
176°E
0.05
0.04
0.03
0.02
0.01
Frontal probability
(a)
el_nino n=581 [-0.0385, 0.0374]
0.04
0.02
0.00
−0.02
−0.04
Values of -δ
(b)
la_nina n=883 [0.0, 0.1271]
(c)
la_nina n=883 [-0.0426, 0.0331]
(d)